Supplementary Information

Electrical charge state identification and control for the silicon vacancy in 4H-SiC

M. E. Bathen[1], A. Galeckas[1], J. Müting[2], H. M. Ayedh[1], U. Grossner[2], J. Coutinho[3], Y. K. Frodason[1], and L. Vines[1]

[1]Department of Physics/ Centre for Materials Science and Nanotechnology, University of Oslo, N-0316 Oslo, Norway
[2]Advanced Power Semiconductor Laboratory, ETH Zürich, Physikstrasse 3, 8092 Zürich, Switzerland
[3]Department of Physics and I3N, University of Aveiro, Campus Santiago,3810-193 Aveiro, Portugal

Supplementary Notes 1: Silicon vacancy-related photoluminescence

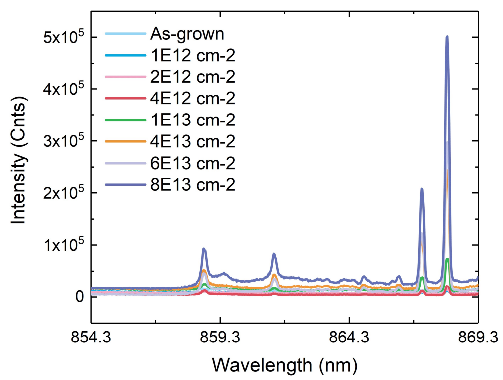

Supplementary Figure 1: Photoluminescence spectra collected at 10K from several 4H-SiC samples proton irradiated to different fluences, focused around the V1 line.

Supplementary Figure 1 displays the PL spectra obtained after proton irradiation to various fluences, revealing the proton fluence dependence of the V1-related luminescence. The V1 and V1' ZPL intensities clearly increase with the proton fluence. The spectra form the basis for the correlation between the V1/V1' emission and the S1/S2 peaks observed by DLTS and shown in Figure 5 of the main text.

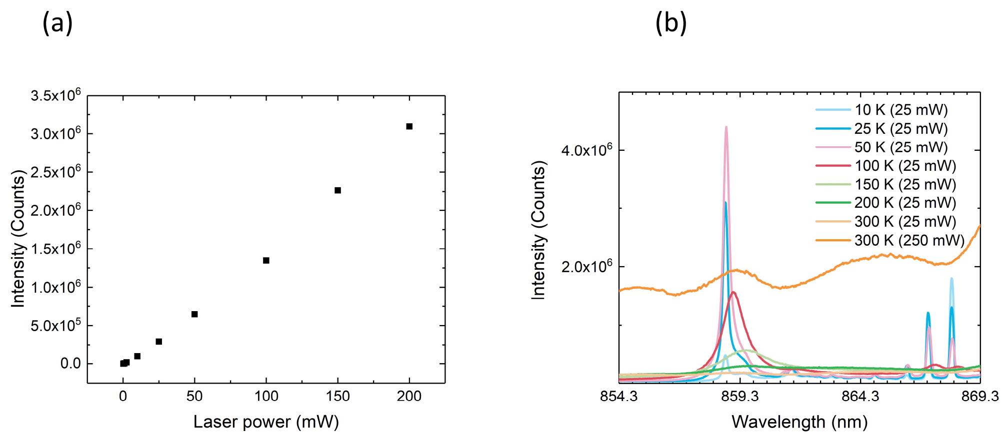

Supplementary Figure 2: (a) Intensity dependence of V1 emission for sample irradiated to a proton fluence of 4E13 cm^{-2}, and (b) temperature dependence of PL in the vicinity of the V1 line for a fluence of 8E13 cm^{-2}.

Supplementary Figure 2(a) demonstrates the intensity dependence of V1 emission for a proton fluence of $4 \times 10^{13}\ \mathrm{cm}^{-2}$. The most commonly employed power of the laser excitation in this work is $25\ \mathrm{mW}$, which is substantially below saturation. For a given excitation beam diameter on the sample surface of ~200µm, the corresponding intensity of such excitation is ~100 W/cm^2, which is by far below what is typically reported for confocal systems, in the 100 kW/cm^2 range. Even at the highest excitation power used in our experiments of $250\ \mathrm{mW}$, the intensity merely reaches ~1kW/cm^2, thus a linear dependence is maintained between the PL intensity and the defect concentration. Supplementary Figure 2(b) displays emission close to the V1 line as a function of temperature. The figure reveals that the intensity of V1 decreases and the signature broadens with increasing temperature. However, it remains clearly visible above liquid nitrogen temperatures, until it becomes difficult to distinguish at temperatures above $200\ \mathrm{K}$.

Supplementary Notes 2: Schottky barrier diode characteristics

Capacitance-voltage

The effect of electric fields on silicon vacancy-related emission was studied using n-type 4H-SiC samples having 10 µm epitaxial layers purchased from Cree, Inc. To enable application of electric fields to the defects, we dipped the samples in 2 % HF to remove the native oxide, and deposited circular Ni contacts using electron beam evaporation to form Schottky barrier diodes (SBDs). The SBDs were 150 nm thick and had diameters of approximately 1 mm, as verified by microscopy.

First, the SBDs were used to determine sample characteristics. By performing capacitance-voltage measurements, we were able to determine the net carrier concentrations in the samples, estimate the depletion region width at different biases, and find the real Schottky barrier height.

Supplementary Figure 3 demonstrates the typical voltage response of an SBD deposited on the n-type proton irradiated 4H-SiC samples studied within this work, with capacitance versus voltage shown in (a) and $1/C^2$ vs voltage shown in (b). Taking the average over eight such CV measurements, we arrived at a mean built-in voltage of 1.5 V, which was later used in the device simulations.

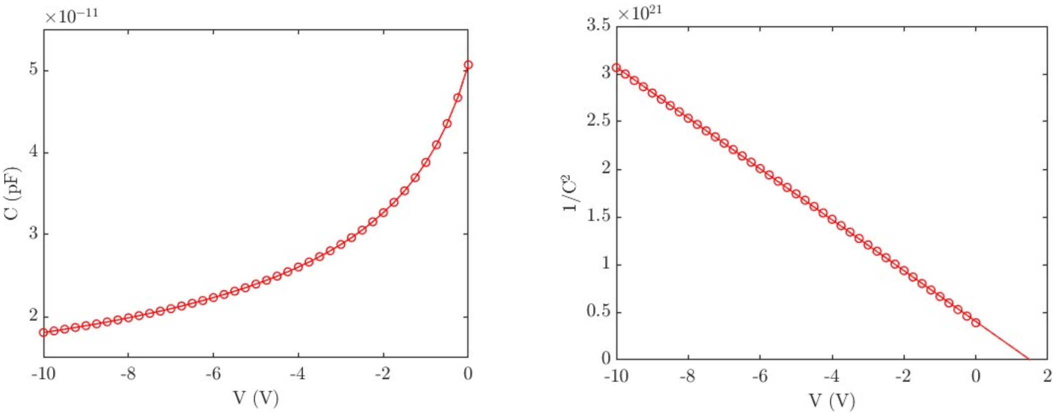

Supplementary Figure 3: representative (a) CV measurement, and (b) $1/C^2$ vs voltage, for a Schottky barrier diode deposited on a n-type 4H-SiC sample proton-irradiated to a fluence of $2 \times 10^{11}\ \mathrm{cm}^{-2}$.

The capacitance of an SBD is given as $C = \frac{\epsilon A}{W}$, where ϵ is the semiconductor permittivity, A is the diode area and W is the depletion region width. W is given by

$W = \sqrt{\frac{2\epsilon(V_{\text{built-in}} - V_{\text{applied}})}{qN_d}}$, where N_d is the donor concentration. The net carrier concentration (N_d) as a function of the depletion region width (W) is estimated from the CV measurement demonstrated in Supplementary Figure 3(a), and plotted in Supplementary Figure 4. As an average value, we estimate that the net carrier concentration in the n-type 4H-SiC samples is approximately $N_d = 1 \times 10^{15}\ \mathrm{cm}^{-3}$. Now that we have an estimate of the built-in voltage and N_d, we can find the Schottky barrier height according to $\Phi_B = V_{\text{bi}} + \frac{E_c - E_{Fs}}{q} = V_{\text{bi}} + 0.2\ \mathrm{V} = 1.7\ \mathrm{V}$.

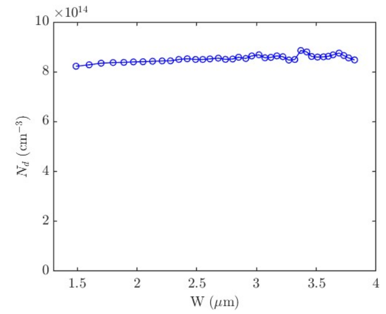

Supplementary Figure 4: Net carrier concentration versus depletion region depth, as estimated from CV measurements obtained from a 4H-SiC sample proton-irradiated to a fluence of $2 \times 10^{11}\ \mathrm{cm}^{-2}$.

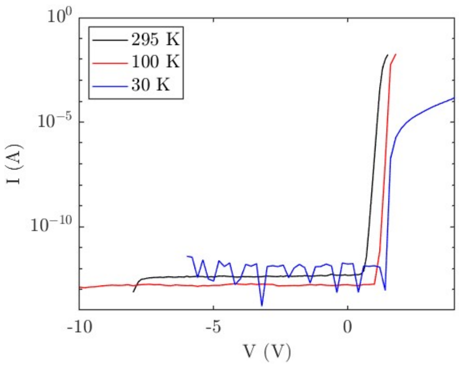

Supplementary Figure 5: Temperature-dependent current-voltage characteristic for a representative SBD deposited onto an n-type 4H-SiC sample proton-irradiated to a fluence of $2 \times 10^{11}\ \mathrm{cm}^{-2}$.

Current-voltage

Supplementary Figure 5 illustrates the temperature-dependent IV characteristics of a representative Schottky diode. The difference is small between the room temperature and the 100 K curves, but increases as the temperature drops to 30 K. However, the diode is clearly rectifying also at a temperature of 30 K. The noise present for the 30 K IV curve can be ascribed to the cryogenic pump.

Electric field

The maximum applied electric field depends on the depletion region width, and thereby the applied bias voltage, according to

$$\xi_0 = -\frac{q}{\epsilon} N_d W.$$

Within this work, the applied electric field cited in Figure 7 of the main text (concerning the Stark effect) refers to the maximum applied electric field, and not the local field experienced by the individual defect.

Forming a Schottky barrier diode on the 4H-SiC sample surface results in an electric field over the depletion region, which is further modified by applying external bias. The electric field strength has been estimated under the depletion approximation and the doping concentration extracted from the CV measurements. Consequently, contributions from local space charge or laser excitation has been assumed to be negligible. In this regard, it is worth noting that no significant change was observed in the measured current during the sub-bandgap excitation performed here.

As defect distribution and concentration within the depletion region differed for different samples, the electric field experienced by each individual defect may differ from the presented electric field values.

Supplementary Notes 3: Field effect on emission from V_{Si} ensembles in 4H-SiC

Effect of built-in field

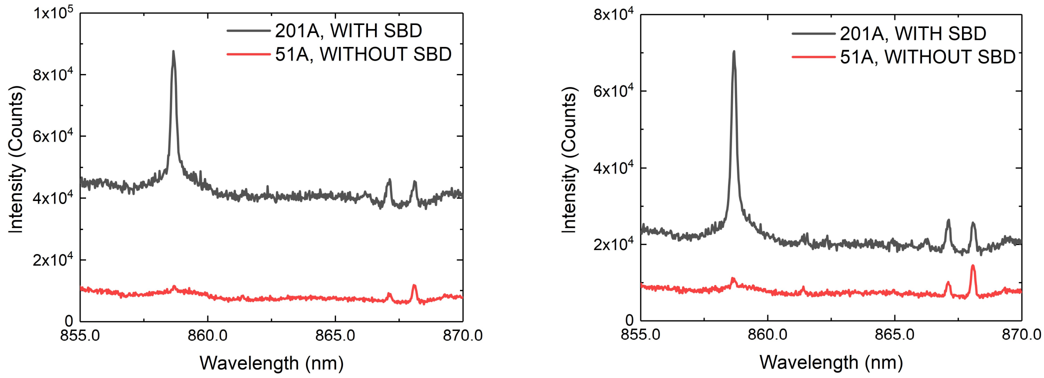

Supplementary Figure 6: Effect of built-in field imposed by Schottky barrier diode on the V1 PL signal originating from V_{Si}^{-1} in two different 4H-SiC samples proton irradiated to a fluence of (a) $1 \times 10^{12}\ \mathrm{cm}^{-2}$ and (b) $2 \times 10^{12}\ \mathrm{cm}^{-2}$.

Supplementary Figure 6 demonstrates how the presence of the SBD drastically increases V1 emission for two different fluences: (a) $1 \times 10^{12}\ \mathrm{cm}^{-2}$, and (b) $2 \times 10^{12}\ \mathrm{cm}^{-2}$. The first fluence is represented in the main text by Figure 2(e), and the second by Figure 2(d). In each case the PL was collected from two different samples: one with and one without SBD, but both irradiated at the same time and to the same fluence. A stands for acquisition and each acquisition lasted 1 second. Indeed, integration over 201 acquisitions does lead to larger peak intensities in total, but affects the background equally. With SBD, we clearly see a much larger V1 peak as compared to the SBD-free case. On the other hand, in the case of a bare implanted surface (without SBD), the spectral contents include both V1' and V1 signatures, as can be observed in Supplementary Figure 7.

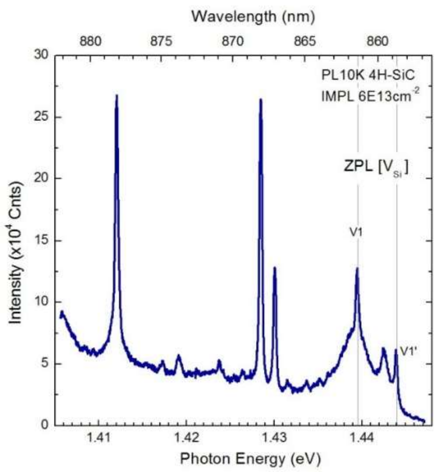

Supplementary Figure 7: PL spectrum obtained at 10 K from proton irradiated epilayer clearly revealing presence of both ZPL V1 lines. Note the prevailing V1 over V1', which is in contrast to what is observed in the case of probing SBD.

The drastic increase demonstrated in Supplementary Figure 7, and in Figure 2(b) of the main text, is larger than expected from geometrical considerations, where the main factor is reflection from the semiconductormetal interface. Hence, an increase no more than a factor two would be expected, while about an order of magnitude is observed. The band bending due to the Schottky barrier must therefore cause the increase.

Effect of external field

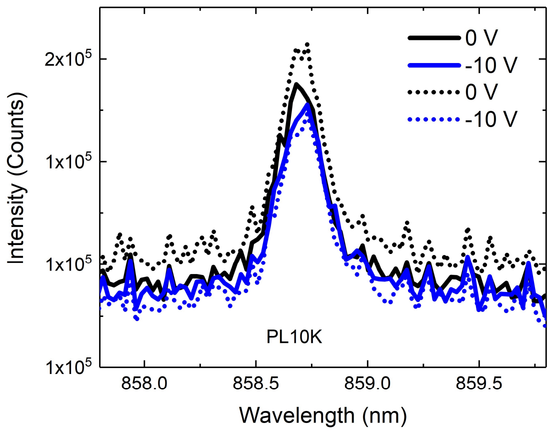

Supplementary Figure 8: Effect of sequential application of -10 V reverse bias on V1’ emission intensity. The sample was proton-irradiated to a fluence of 1×10^{12} cm^{-2}.

Supplementary Figure 8 demonstrates that while intensity modulation of V1’ is still obtainable for larger biases, here for -10 V, the modulation depth becomes less predictable.

Proton fluence dependence

As mentioned in the manuscript, we observe a pronounced proton fluence dependence for the V1’ emission modulation. For the lower proton fluence of 1×10^{12} cm^{-2}, we can modulate the photon counts by up to 20 %. For the higher proton fluence of 2×10^{12} cm^{-2}, the modulation is twice as large and exceeds 45 % (see Figure 2 of the main text).

Supplementary Discussion 1: DLTS investigation of the S1 peak

The DLTS spectra [1] were obtained using a DLTS setup as described in Ref. [2]. Previous works have established that the measured capture cross sections for S1 and S2 differ from the apparent ones, and are $\sigma = 8 \times 10^{-1}\ \ \mathrm{cm}^{-2}$ for S1, and $\sigma = 3 \times 10^{-15}\ \mathrm{cm}^{-2}$ for S2 [3]. The significant difference of more than an order of magnitude resonates with S1 corresponding to the (2-/3-) transition, as a large electron repulsion would be associated with V_{Si} capturing the additional electron.

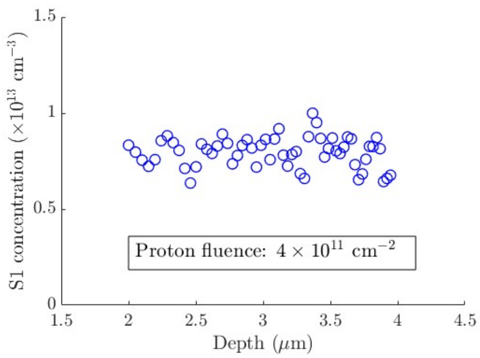

Supplementary Figure 9: S1 concentration depth profile for a proton irradiation fluence of 4×10^{12} cm^{-2}, demonstrating a uniform trap distribution throughout the depletion region.

Supplementary Figure 9 demonstrates that the S1 concentration is uniform throughout the depletion region, as expected for a primary point defect (such as the silicon vacancy) after proton irradiation. The concentration versus depth profiles of the S1 defect was determined according to the relation [4]

$$N_t(x) = \left(\frac{qW^2N_d}{\epsilon}\right) N_d(x) \frac{\partial\left(\frac{\Delta C}{C}\right)}{\partial V},$$

where N_t is the defect concentration, q the elementary charge, W the depletion region depth, N_d the concentration of ionized donors, ϵ the semiconductor permittivity, and the last factor is the derivative of the DLTS signal versus voltage. As only the uniformity of the S1 concentration profile was to be considered, we disregarded the lambda correction [5].

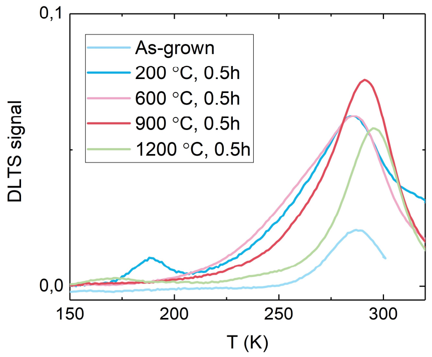

Supplementary Figure 10: Temperature dependence of the S1 defect center.

Supplementary Figure 10 shows the temperature dependence of the S center, as represented by the S1 peak. S1 is not present in as-grown material, appears after ion implantation (here using $4\ \mathrm{MeV}$ Carbon ions to a fluence of $4 \times 10^{8}\ \mathrm{cm}^{-2}$) and annealing at $200\ ^{\circ}\mathrm{C}$ for 30 minutes in air. Annealing the sample at $600\ ^{\circ}\mathrm{C}$ or above removes the S1 peak, perfectly in line with behavior commonly associated with the silicon vacancy.

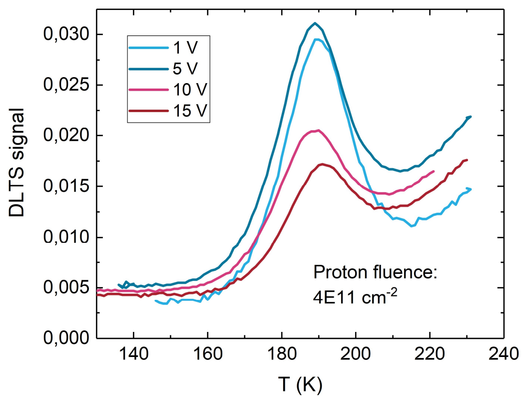

Supplementary Figure 11: Voltage dependence of the S1 peak (normalized), displaying the absence of the Poole-Frenkel effect, indicating an acceptor-like nature for the S1 defect.

Supplementary Figure 11 shows the voltage dependence of the S1 peak, demonstrating no Poole Frenkel effect and therefore an acceptor-like behavior of the S1 defect center.

Supplementary Discussion 2: Determining silicon vacancy concentrations

Knowing that the S center has a uniform concentration profile in the proton irradiated samples, its concentration can be determined according to

$$N_t = 2N_d \frac{\Delta C}{C_r},$$

where ΔC is the capacitance transient in the peak. For S1 this is relatively straightforward, while for S2 and $Z_{1/2}$ the overlap between the two peaks renders extraction of the peak amplitude difficult. Accordingly, the DLTS spectrum was simulated to extract all trap concentrations for each proton irradiation fluence, using known parameters for the activation energy and capture cross section [3]. The lambda-effect [5] was accounted for when determining the trap concentrations.

The V1/V1' emission intensities for each proton fluence were determined after a linear baseline subtraction.

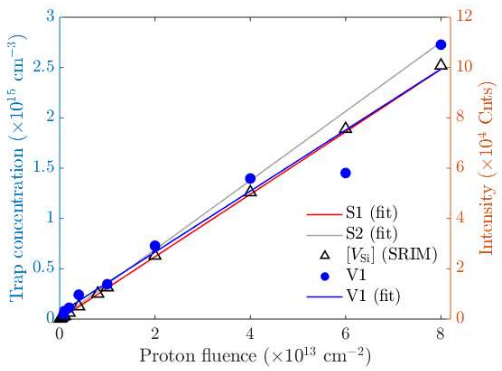

Supplementary Figure 12: S center concentration, and V1 emission intensity, dependence on the proton fluence.

Supplementary Figure 12 illustrates the same behavior as in Figure 5 of the main paper. The main features summarized by the figure that support the assignment of V_{Si} as the S center are:

- The S1 and S2 concentrations increase linearly with the proton fluence, as expected for primary point defects such as vacancies that are created by ion implantation in the dilute limit.
- When fitting the dynamic annealing factor to the known carbon vacancy concentration, the S center concentrations match those predicted for V_{Si} using SRIM very well.

- The extracted dynamic annealing factor says that 3 % of the Si vacancies survive ion implantation and the subsequent heat treatment. The factor of 3 % falls within the range we expect for primary point defects created by ion implantation.
- The slopes of the proton fluence dependence of the S center, the V1 center, and V_{Si} as predicted by SRIM, overlap very well, as seen by Supplementary Figure 12.

Supplementary Methods 1: SRIM simulations of proton irradiation

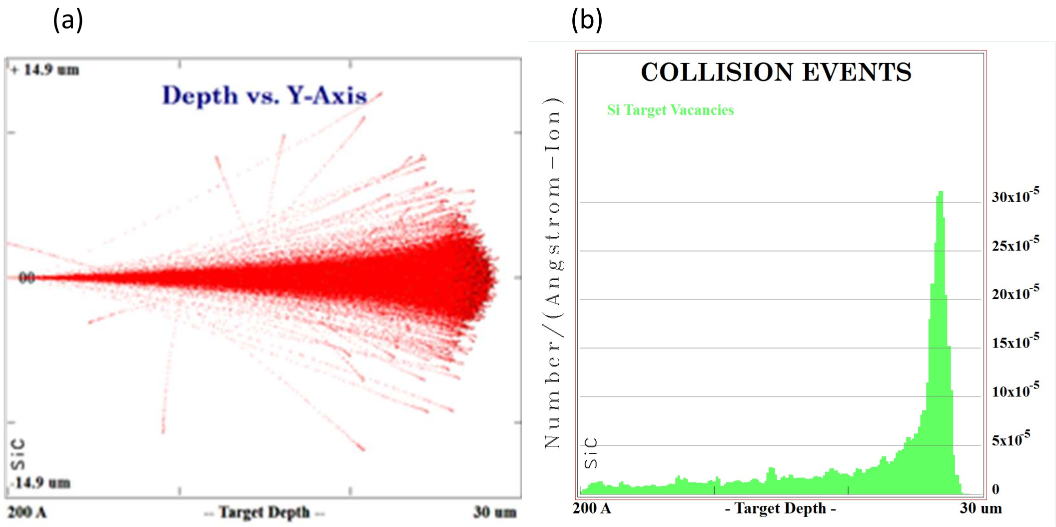

Supplementary Figure 13: Generated silicon vacancies follow 1.8 MeV proton irradiation, as estimated using the SRIM code, showing (a) the lateral distribution and ion trajectories, and (b) the average vacancy generation as a function of target depth.

SRIM 2013 [6] was used to provide an initial estimate of both the target silicon vacancies, and their projected range, following irradiation with 1.8 MeV protons to different fluences. The collision events of the protons are illustrated in Supplementary Figure 13(a), with Supplementary Figure 13(b) showing the predicted Si vacancy concentration profile. We find that the Si vacancy peak is situated approximately 27 µm into the sample, with the near-surface defect tail being approximately uniform.

Moreover, the SRIM simulations were used to estimate the expected silicon vacancy concentration after irradiation to varying proton fluences. By comparing the SRIM simulation to the DLTS measurements of the $Z_{1/2}$ level assigned to the well-known carbon vacancy, we were able to estimate the number of silicon and carbon vacancies surviving dynamic annealing during ion implantation, and the 300 °C post-irradiation anneal, at 3 %.

Supplementary Methods 2: Laplace-DLTS investigation of the S1 peak

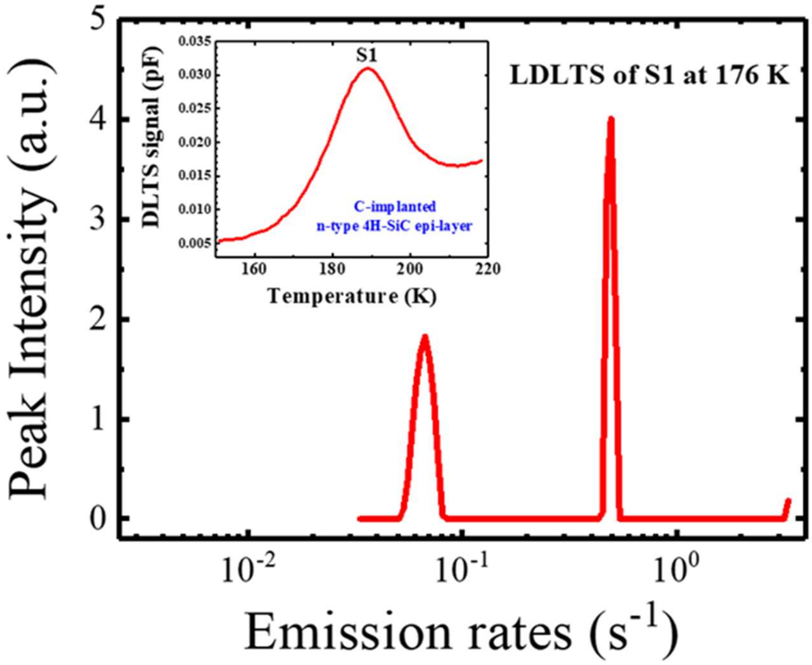

Supplementary Figure 14: Laplace-DLTS measurement of the S1 deep center at 176 K in n-type 4H-SiC epi-layer implanted by C-ions. The inset Supplementary Figure hows the conventional DLTS spectrum of S1 in the same sample. The LDLTS measurement clearly separates the signals from two closely separated deep levels of S1 which are indistinguishable by conventional DLTS.

If two closely spaced energy levels have similar emission rates (time constants), it is extremely difficult to distinguish these levels by means of conventional DLTS, where two closely overlapping peaks will be monitored as a single broad peak in the DLTS spectra. A numerical methods using Laplace transformation was developed to better separate the interlaced emission rates of these close energy levels from the recorded capacitance transients; this is known as Laplace DLTS (LDLTS) [7]. This powerful technique has been successfully employed to resolve overlapping defects in semiconductors [8]. The relevant mathematical details are rather complex and to facilitate utilizing LDLTS, the numerical calculations are done by a software procedure called CONTIN [9], based on the so-called Tikhonov regularization method [10]. LDLTS measurements are very sensitive to the temperature change, and LDLTS systems use isothermal measurements with high thermal stability, maintaining the temperature at the range ± 0.02 K during the measurement. The Laplace DLTS method analyzes emission rates at a specific temperature and provides a spectrum of capacitance transient signal against the emission rate rather than against temperature. In order to extract the energy positions of closely spaced deep levels, an Arrhenius plot can be produced by the repetition of LDLTS measurements at a number of different temperatures.

LDLTS Measurement details

In LDLTS measurements, capacitance transients were recorded at a series of temperatures; 176, 179, 182, 185, 188, 191, and 194 K, by keeping the temperature stability within ±0.02 K. Reverse bias of -5V and a filling pulse voltage to 0 V of 50 ms width were applied. The transient length (scan time) has been adjusted at each measurement until the maximum amplitude of the capacitance transient is displayed and a full shape of saturated transient is shown. During the LDLTS measurements, each capacitance transient consisted of 10^6 points and the recorded transient for Laplace transform was obtained by averaging a total of 500 - 1000 capacitance transients, in order to increase the signal-to-noise ratio. The Laplace transform was then computed from the averaged transient and the raw data of 10^6 points were compacted to 1000 points representing the entire transient using CONTIN software that employs Tikhonov regularization.

In this study, the high energy resolution LDLTS technique was employed in an attempt to resolve the emission rates of closely spaced deep states of S1 defect that are attributed to the hexagonal and cubic contributions of the silicon vacancy (V_{Si}) in 4H-SiC epilayers implanted by C ions (4 MeV, C fluence of 6E8 cm^{-2}). Indeed, two distinct signals of the S1 peak could be clearly resolved, as illustrated in Supplementary Figure 14 for LDLTS measurement performed at sample temperature 176 ± 0.02 K. The conventional DLTS spectrum of S1 peak is shown as an inset at the top of Supplementary Figure 14. The broad peak centered at 188 K for the DLTS rate window ($(640\ ms)^{-1}$) is due to electron emissions from both the hexagonal and the cubic sites of V_{Si}.

LDLTS spectra of S1 deep levels at different temperatures are shown in Figure 4(b) in the main article, and Figure 4(c) displays Arrhenius plots of the two LDLTS peaks of the S1contributions. The energy separation for the two contributions to S1 deduced using Laplace-DLTS is 0.04 eV, as seen in Figure 4(c), is somewhat below the 0.1 eV estimated by hybrid DFT calculations. However, the difference of 0.06 eV is well within the error bar of both techniques. Although the two peaks in Supplementary Figure 14 have different peak intensities, their integrated areas are approximately identical. During irradiation, both *h* and *k* silicon vacancies are formed. As the two configurations of V_{Si} differ in formation energy by only 0.1 eV in most charge states (see Figure 3 of the main text), high-energy proton irradiation is expected to form approximately equal amounts of both defect types. Accordingly, the Laplace-DLTS study of the S1 peak reinforces our belief that the S1 defect center in fact originates from the (2-/3-) charge-state transition of V_{Si}.

Supplementary Methods 3: Device simulations

The device simulations yielding band structures were performed using Sentaurus Device from Synopsys. For simplicity reasons, the geometry (4H-SiC, 1 x 10 µm, $N_{D,const}$ = 1E15 cm^{-3}) was created with Sentaurus Editor, only taking the n-type epilayer into account. Simulations of the full device including the substrate showed identical results, but consumed much more computational time. Within Sentaurus Device the Schottky contact was introduced with a barrier height of 1.7 eV. In order to achieve a realistic simulation, the following physical models were used with specific 4H-SiC parameters: incomplete ionization of nitrogen, doping dependence of the mobility, Auger and Shockley-Read-Hall recombination. Constant defect levels at E = 0.4 eV and E = 0.7 eV (to emulate the (-2/-3) and (-1/-2) charge state transitions of the V_{Si}, respectively) with a concentration of C = 1E13 cm^{-3} were additionally included. To achieve convergence at lower temperatures a very fine mesh was used.

Supplementary Figure 15 shows several band diagrams of the Schottky contact for varying biases and temperatures.

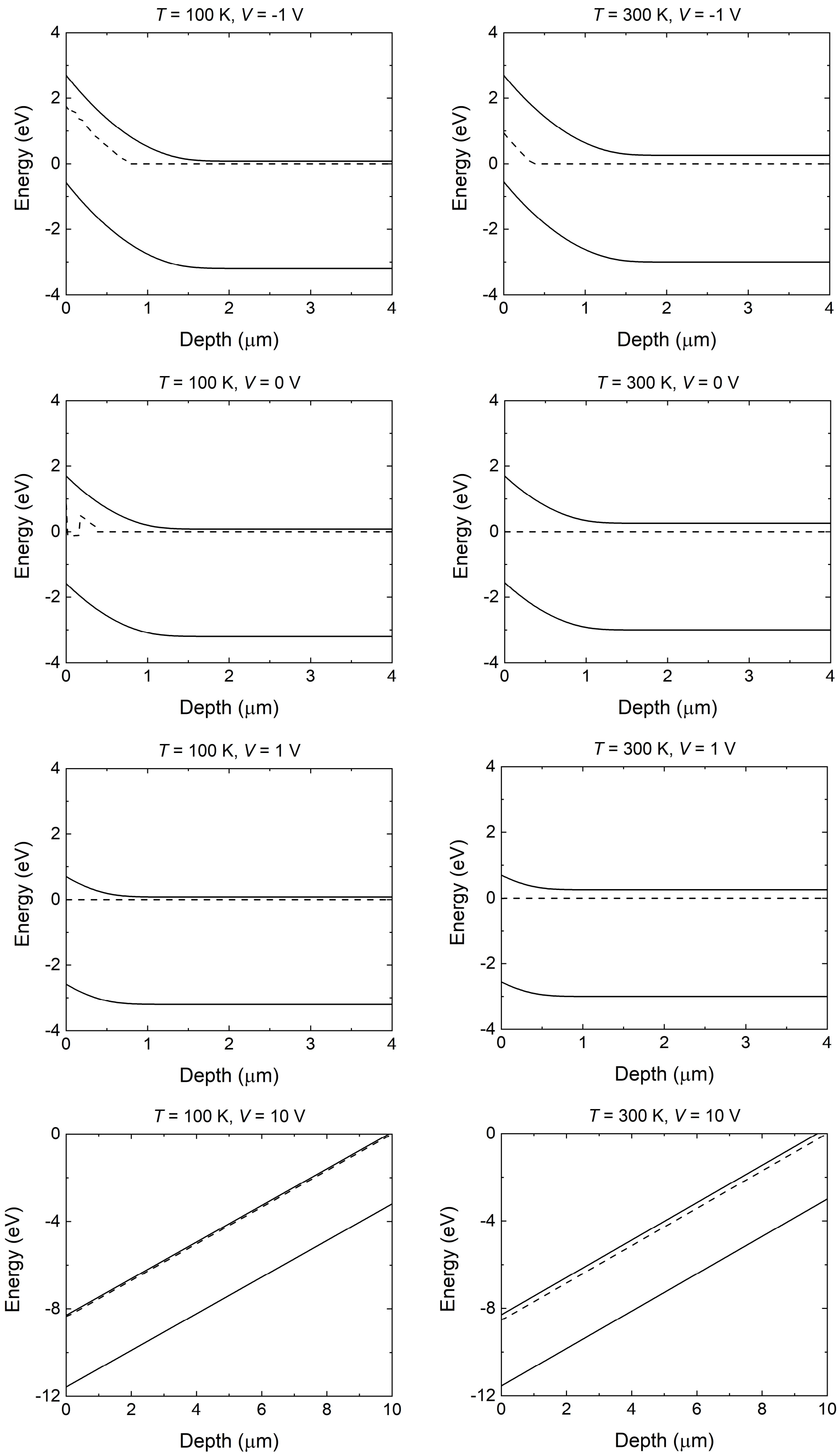

Supplementary Figure 15: Simulated band diagrams with different biases for T = 100 K (left) and T = 300 K (right). The upper solid line is the conduction band, the lower solid line the valence band and the dashed line the Fermi level. Zero depth corresponds to the Schottky contact.

Supplementary Figure 16 and 17 show the distribution of the absolute electric field and the electron density for small biases at T = 300 K. The current voltage relation of the Schottky diode at T = 300 K can be seen in Supplementary Figure 18. A leakage current of around -10^{-23} A can be estimated, as shown in Supplementary Figure 18.

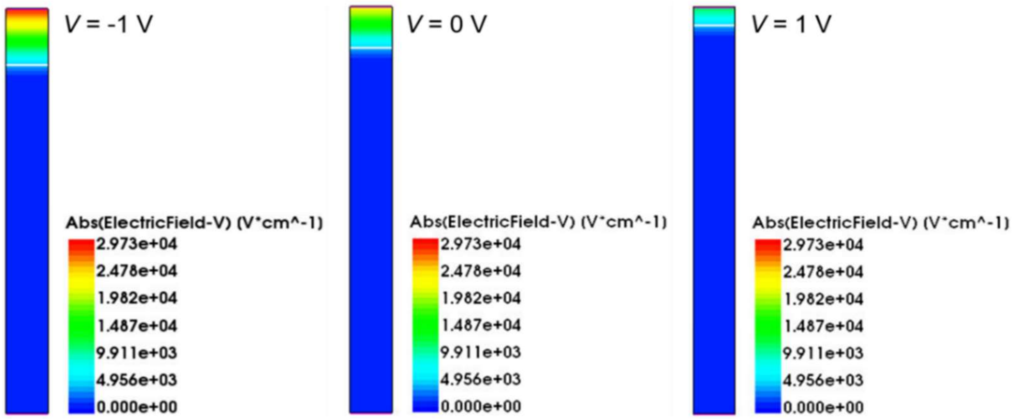

Supplementary Figure 16: Absolute electric field within simulated structure for different biases at T = 300 K. The Schottky contact is at the top of the structure, which is 1 µm x 10 µm.

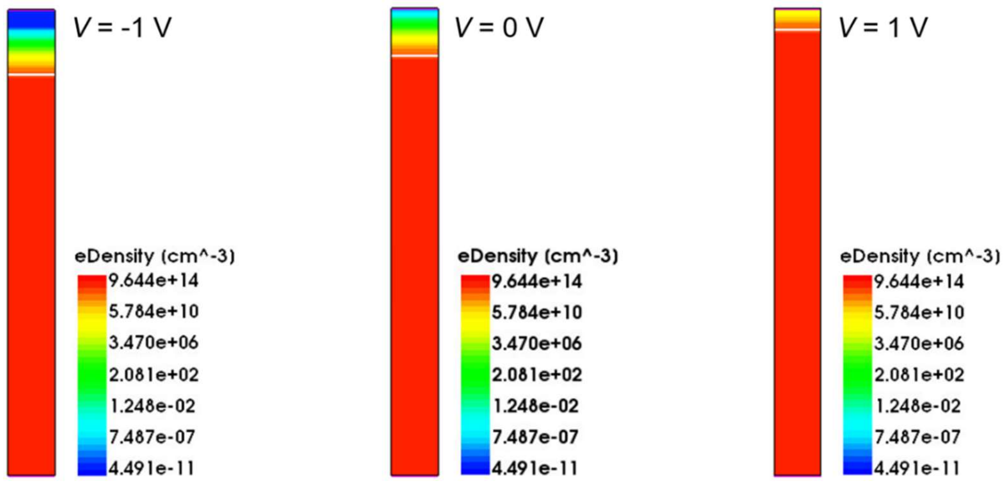

Supplementary Figure 17: Electron density within simulated structure for different biases at T = 300 K. The Schottky contact is at the top of the structure, which is 1 µm x 10 µm.

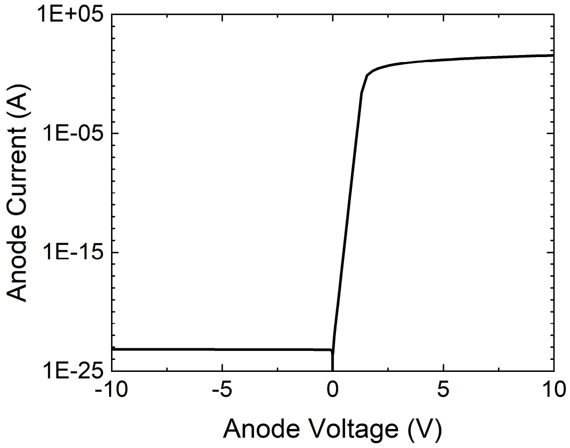

Supplementary Figure 18: Anode current over voltage of the Schottky diode at T = 300 K. The simulation uses an appropriate area factor to scale the simulation.

Supplementary References

[1] D. V. Lang, Journal of Applied Physics **45**, 3023 (1974).

[2] B. G. Svensson, K.-H- Rydén, and B. M. S. Lewerentz, Journal of Applied Physics **66**, 1699 (1989).

[3] M. L. David, G. Alfieri, E. M. Monakhov, A. Hallén, C. Blanchard, B. G. Svensson and J. F. Barbot, Journal of Applied Physics **95**, 4728 (2004).

[4] P. Blood and J. W. Orton, The Electrical characterization of Semiconductors: Majority Carriers and Electron States (Academic Press Limited, London, 1992).

[5] S. D. Brotherton, Solid-State Electronics **26**, 987 (1983).

[6] J. F. Ziegler, M. Ziegler, and J. Biersack, Nuclear Instruments and Methods in Physics Research Section B: Beam Interactions with Materials and Atoms **268**, 1818 (2010).

[7] L. Dobaczewski, P. Kaczor, I. D. Hawkins, and A. R. Peaker, J. Appl. Phys. **76**, 194 (1994).

[8] L. Dobaczewski, A. R. Peaker, and K. Bonde Nielsen, J. Appl. Phys. **96**, 4689-4728, (2004).

[9] S. W. Provencher, Comput. Phys. Commun. 27, 213 (1982).

[10] C. W. Groetsch, The Theory of Tikhonov Regularisation for Fredholm Equations of the First Kind (Pitman Advanced Pub, London, 1984).